

Ideal Spin-Orbit-Free Dirac Semimetal and Diverse Topological Transitions in Pr_8CoGa_3 Family

Manabu Sato,¹ Juba Bouaziz,² Shuntaro Sumita,^{3,4,5} Shingo Kobayashi,⁶
Ikuma Tateishi,⁶ Stefan Blügel,² Akira Furusaki,^{5,6} and Motoaki Hirayama^{1,6,*}

¹*Department of Applied Physics, University of Tokyo, Tokyo 113-8656, Japan*

²*Peter Grünberg Institut and Institute for Advanced Simulation, Forschungszentrum Jülich and JARA, D-52425 Jülich, Germany*

³*Department of Basic Science, The University of Tokyo, Meguro, Tokyo 153-8902, Japan*

⁴*Komaba Institute for Science, The University of Tokyo, Meguro, Tokyo 153-8902, Japan*

⁵*Condensed Matter Theory Laboratory, RIKEN CPR, Wako, Saitama 351-0198, Japan*

⁶*RIKEN Center for Emergent Matter Science, Wako, Saitama 351-0198, Japan*

(Dated: January 26, 2024)

We propose from first-principles calculations that spin-orbit-free materials in the $RE_8\text{CoX}_3$ group ($RE =$ rare earth elements, $X = \text{Al, Ga, or In}$) are ideal spinless Dirac semimetals whose Fermi surfaces are fourfold degenerate band-crossing points (without including spin degeneracy). Despite the lack of space inversion symmetry in these materials, Dirac points are formed on the rotation-symmetry axis due to accidental degeneracies of two bands corresponding to different 2-dimensional irreducible representations of C_{6v} group. The surface states have two midgap bands emanating from the projection in the surface Brillouin zone of the bulk Dirac points, in accordance with nontrivial Zak phases for each glide sector. We also investigate, through first-principles calculations and effective model analysis, various phase transitions caused by lattice distortion or elemental substitutions from the Dirac semimetal phase to distinct topological semimetallic phases such as nonmagnetic linked-nodal-line and Weyl semimetals (characterized by the second Stiefel-Whitney class) and ferromagnetic Weyl semimetals.

I. INTRODUCTION

Topological semimetals are a fascinating group of materials with degeneracies between valence and conduction bands that exhibit intriguing properties in the bulk and at the surface, e.g. due to interference effects between the electronic states around the degeneracy points [1]. There exist various types of topological semimetals in real materials including Weyl [2–6], Dirac [7–14], and nodal-line semimetals [15–17], for spinless and spinful systems. Here spinless systems refer to materials with negligibly weak spin-orbit couplings (SOC), while spinful systems have strong SOC; we will ignore the spin degrees of freedom when we consider spinless systems below.

The recent development of the representation theory of electronic energy bands, such as symmetry-based indicators [18] and topological quantum chemistry [19], has enabled the exhaustive search over crystal databases for topological materials [20–25]. Nevertheless, the comprehensive classification and detailed characterization of topological semimetals are still lacking. For example, no material realization of spinless Dirac semimetals with a quadruple degeneracy between the valence and conduction bands has been discovered to the best of our knowledge [26]. In fact, the irreducible representations (irreps) of valence bands at high symmetry points alone cannot tell us whether the material in question is an ideal semimetal without superfluous Fermi surfaces of finite area, while they can determine the presence of nodes and their degree of degeneracy [20–25, 27]. Moreover, for spinless systems, there is currently no guiding principle for the realization of band inversion, which is essential for the design of topological insulators and topological semimetals, in contrast to the

spinful systems, where the band inversion can be achieved by strong SOC. Thus, the study of spinless topological materials lags behind that of spinful ones.

In materials with strong SOC (spinful systems), there are two distinct classes of Dirac semimetals [1, 28, 29]. In one class of Dirac semimetals, a pair of Dirac points is formed due to an accidental band crossing of two different 2-dimensional irreps on a high-symmetry line, as seen in Na_3Bi [8, 9] and Cd_3As_2 [10–14]. In the second class of Dirac semimetals with nonsymmorphic symmetry, such as $\beta\text{-BiO}_2$ [7], a Dirac point appears as a 4-dimensional irrep at a high-symmetry point on the boundary of the Brillouin zone (BZ). These two classes of Dirac semimetals are also expected to exist in spinless systems, and the space groups that can realize each class are listed in Ref. [30].

In this paper we study the first class of spinless Dirac semimetals and its material realization. We focus on the space groups with C_{6v} symmetry that accommodates two 2-dimensional irreps along a high symmetry line in the BZ. In addition to the space group considerations, we utilize the chemical bonding perspective to design ideal Dirac semimetals. We choose elements with similar electronegativity that form covalent bonds, which we expect to result in the reduction of the density of states (DOS) at the Fermi energy.

Our study reveals that materials within the $RE_8\text{CoX}_3$ group ($RE =$ rare earth elements, $X = \text{Al, Ga, or In}$) exhibit the spinless Dirac semimetal phase with nontrivial topological properties. These materials have C_{6v} symmetry on the high symmetry line in the BZ. We will begin by discussing these materials' crystal structure and their symmetry. Taking Y_8CoIn_3 as an example, we will present the bulk electronic structure and the characterization of its topology, and describe the surface states and their correspondence to the bulk topological invariant. Next, we will show the diverse topological phase transitions caused by symmetry reductions in the target ma-

* hirayama@ap.t.u-tokyo.ac.jp

terials, from the Dirac semimetallic phase to nodal-line and Weyl semimetallic phases characterized by the second Stiefel-Whitney (SW) class. Finally we will consider the substitution of rare earth elements to introduce strong SOC and discuss possible magnetic properties.

II. RESULTS

A. Electronic band structure

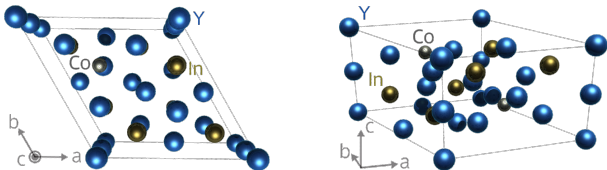


FIG. 1. Crystal structure of Y_8CoIn_3 . The blue, gray, and gold balls represent Y, Co, and In atoms, respectively.

Among the ternary compounds RE_8CoX_3 (RE = rare earth elements, X = Al, Ga, or In), the experimentally synthesized compounds all show a hexagonal crystal structure with the nonsymmorphic space group $P6_3mc$ (No. 186) [31–33]. This structure lacks space inversion symmetry and has a polarization along the c -axis. Figure 1 shows the crystal structure of Y_8CoIn_3 [32], where the measured lattice constants are $a = b = 10.3678 \text{ \AA}$ and $c = 7.0069 \text{ \AA}$. The crystal structure is three-dimensional and the composition is primarily made up of Y elements. The space group has a sixfold screw symmetry around the z axis $\{C_{6z}|00\frac{1}{2}\}$, a mirror symmetry with respect to the yz plane $\{M_x|000\}$, and a glide symmetry with respect to the zx plane $\{M_y|00\frac{1}{2}\}$, where the z direction is taken to be along the c -axis. As a result, the little co-group C_{6v} is formed along the k_z axis (Γ -A line in the BZ).

Figure 2(a) shows the electronic band structure of Y_8CoIn_3 calculated in the absence of the SOC, with the corresponding bulk BZ shown in Fig. 2(b). Clearly, Y_8CoIn_3 is an ideal semimetal with the band crossing along the Γ -A line. The Fermi surface of this semimetal consists of two Fermi points on the k_z axis that are related by time reversal symmetry. The density of states shown in Fig. 2(c) suggests that the bands near the Fermi level originate mainly from the Y $4d$ orbitals, the Co $3d$ orbitals, and the In $5p$ orbitals. Even though Y_8CoIn_3 is composed of metallic elements, covalent bonds are formed between the Y $4d$, Co $3d$, and In $5p$ orbitals [34], resulting in semimetallic density of states. In addition to these atomic orbital states, the bands in the immediate vicinity of the Fermi level also originate from three interstitial states near the Co atoms [Fig. 2(d)], which are related to each other by the threefold rotational symmetry around the Co atoms.

Along the Γ -A line, there is a little co-group C_{6v} . This group has two distinct 2-dimensional irreps, Δ_5 and Δ_6 , which are distinguished by eigenvalues of the screw symmetry around the z axis. This situation is similar to a benzene molecule with C_{6v} , where the highest occupied molecular orbital (HOMO)

and lowest unoccupied molecular orbital (LUMO) have double degeneracy of different irreps. By contrast, C_{3v} and C_{4v} symmetries cannot have two distinct types of 2-dimensional irreps in spinless systems. The two bands that intersect along the Γ -A line belong to the two different 2-dimensional irreps Δ_5 and Δ_6 [Fig. 2(a)]. These bands cannot hybridize, and their crossing points are fourfold degenerate Dirac points (without counting the spin degeneracy). When the SOC is turned on, the system becomes a spinful Dirac semimetal. The SOC's magnitude at the Dirac point can be adjusted from 20 meV to 75 meV through the elemental substitutions (see Sec. II C 2 and Appendix B).

Figure 2(e) shows the 3-dimensional picture of the band structure around the Dirac point in the $k_x = 0$ plane, calculated without the SOC. We see that the band dispersion around the Dirac point is linear in all directions. As already mentioned, both the valence and the conduction bands are doubly degenerate on the k_z axis (Γ -A line), which is indicated by the black lines in the Fig. 2(e). These degeneracies are lifted away from the k_z axis. To see this, we construct a low-energy $4 \times 4 k \cdot p$ Hamiltonian up to the second order in k around the Dirac point. We find that the two-fold degenerate valence and conduction bands split into four bands, except along the nodal lines marked in white in Fig. 2(e), where either valence or conduction band is two-fold degenerate; we will discuss these nodal lines in more detail below. These features are different from the band structure of spinful Dirac semimetals with spatial inversion symmetry, such as Na_3Bi , where the bands are Kramers degenerate throughout the BZ.

Next, we discuss the topological invariants that characterize the bulk states of Y_8CoIn_3 . The Zak phase along the x -axis

$$\theta(k_y, k_z) = -i \sum_n^{\text{occ.}} \oint dk_x \langle u_n(\mathbf{k}) | \frac{\partial}{\partial k_x} | u_n(\mathbf{k}) \rangle \quad (1)$$

is quantized to either 0 or $\pi \pmod{2\pi}$ due to the mirror symmetry about the yz plane. This means that the Wannier functions are located at mirror-symmetric positions. We find that the nontrivial topology of the bulk states of Y_8CoIn_3 is characterized by the Zak phase $\theta(0, k_z)$ calculated in the $k_y = 0$ plane. The $k_y = 0$ plane is invariant under the glide operation with respect to the zx plane, and the wavefunctions in this plane can be chosen to be eigenstates of the glide operation. We classify the occupied bands in the $k_y = 0$ plane into two sectors according to the sign of the eigenvalues of the glide operation, and calculate the Zak phases for each sector. As shown in Fig. 2(f), the Zak phases change from 0 to π at the Dirac point in both sectors. Note that the Zak phases calculated from all occupied bands have no jump of π at the Dirac point, since the sum of the Zak phases for each sector is 0 $\pmod{2\pi}$ at all k_z .

As shown in Fig. 2(e), there are lines of degeneracies between two valence bands and between two conduction bands, which are connected to the Dirac point. These nodal lines are found not only on the k_z axis but also on the mirror or glide planes. Figure 3 shows the color maps of the energy difference between the two highest valence bands and between the two lowest conduction bands of Y_8CoIn_3 . The calculations are

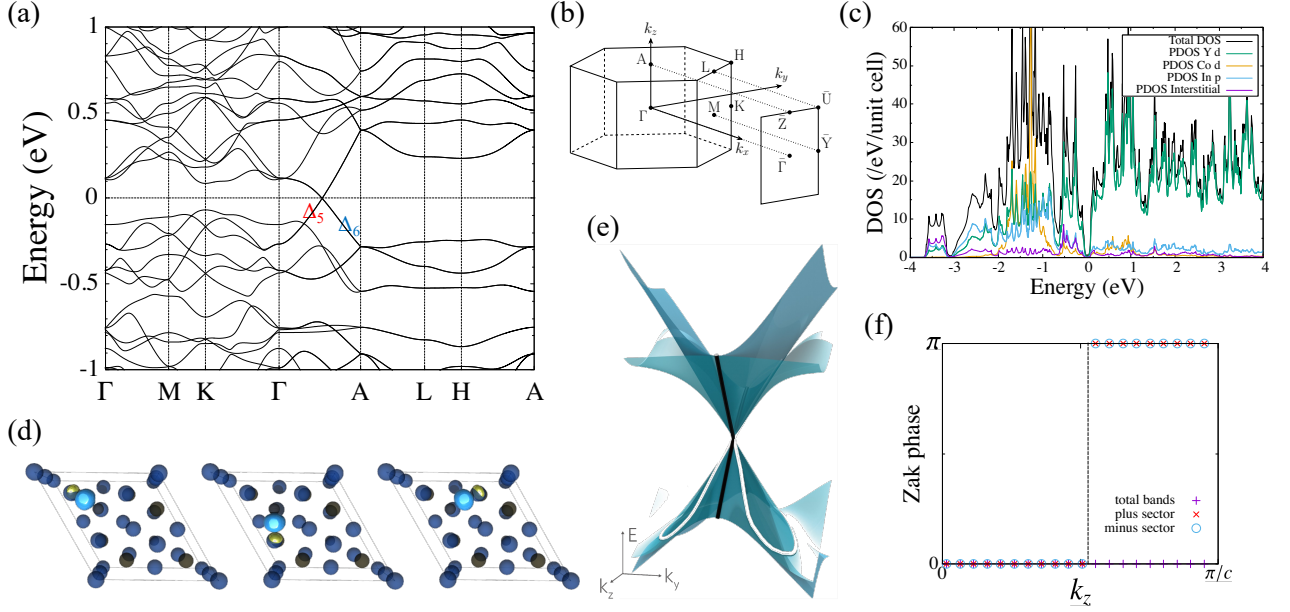


FIG. 2. The electronic structure of Y_8CoIn_3 calculated without the SOC. (a) The electronic band structure of Y_8CoIn_3 calculated by the generalized gradient approximation (GGA). The irreps of the two bands forming the Dirac point in the Γ -A line are shown. The energy is measured from the Fermi level. (b) The bulk BZ and the projected surface BZ for the (1000) surface. (c) The total and partial density of states (PDOS) calculated with the Wannier functions. (d) The interstitial Wannier functions near the Co atoms. The differently colored surfaces represent isosurfaces of opposite sign. (e) The 3-dimensional band structure around the Dirac point calculated in the $k_x = 0$ plane. The black (white) lines represent degeneracies between the valence bands or between the conduction bands on (off) the k_z axis. (f) The Zak phases along the x axis for each glide sector. The dashed line represents the coordinate of the Dirac point.

performed in the mirror invariant plane $k_x = 0$ and the glide invariant plane $k_y = 0$. All four panels show the degeneracy of the bands forming 2-dimensional irreps on the k_z axis. While no additional band degeneracy is found in the $k_y = 0$ plane [Figs. 3(c) and (d)], the two highest valence bands [Fig. 3(a)] and two lowest conduction bands [Fig. 3(b)] of Y_8CoIn_3 have nodal lines in the $k_x = 0$ plane extending from the Dirac point ($k_z^D \approx 0.237 \text{ \AA}^{-1}$) to the diagonal directions, $k_z > k_z^D$ in (a) and $k_z < k_z^D$ in (b).

These properties are explained using the effective $k \cdot p$ Hamiltonian expanded around the Dirac point up to the second order in k . The effective Hamiltonian has the form

$$\begin{aligned}
 H(\mathbf{k}) = & c_1 k_z \Gamma_{0,0} + c_2 k_z \Gamma_{3,0} + c_3 (k_x \Gamma_{2,0} - k_y \Gamma_{1,2}) \\
 & + c_4 (k_x \Gamma_{1,0} + k_y \Gamma_{2,2}) + c_5 (k_x^2 + k_y^2) \Gamma_{0,0} \\
 & + c_6 k_z^2 \Gamma_{0,0} + c_7 [(k_x^2 - k_y^2) \Gamma_{3,3} - 2k_x k_y \Gamma_{0,1}] \\
 & + c_8 (k_x k_z \Gamma_{2,0} - k_y k_z \Gamma_{1,2}) + c_9 (k_x k_z \Gamma_{1,0} + k_y k_z \Gamma_{2,2}) \\
 & + c_{10} (k_x^2 + k_y^2) \Gamma_{3,0} + c_{11} k_z^2 \Gamma_{3,0} \\
 & + c_{12} [(k_x^2 - k_y^2) \Gamma_{0,3} - 2k_x k_y \Gamma_{3,1}], \quad (2)
 \end{aligned}$$

where the Γ matrices are the direct products of the Pauli matrices σ_i ($i = 1, 2, 3$) and a 2×2 unit matrix σ_0 , i.e. $\Gamma_{i,j} = \sigma_i \otimes \sigma_j$. This Hamiltonian has a sixfold rotational symmetry around the z axis $D(C_{6z})H(\mathbf{k})D(C_{6z})^\dagger = H(C_{6z}\mathbf{k})$ [$D(C_{6z}) = -(\Gamma_{3,0} + i\sqrt{3}\Gamma_{0,2})/2$], and a mirror symmetry about the zx plane $D(M_y)H(\mathbf{k})D(M_y)^\dagger = H(M_y\mathbf{k})$ [$D(M_y) = \Gamma_{0,3}$], hence it has C_{6v} symmetry. Note that a previous study [30] has

also systematically constructed the $k \cdot p$ theory in *linear order* in k , whereas our Hamiltonian in Eq. (2) takes into account the *second-order* terms that are crucial for the following discussions. The band structure obtained by first-principles calculations is well fitted in the neighborhood of the Dirac point by the Hamiltonian in Eq. (2), and the obtained parameters are presented in Appendix C. The eigenvalues of $H(\mathbf{k})$ in the $k_x = 0$ plane are

$$\begin{aligned}
 E(0, k_y, k_z) = & [c_5 + (-1)^{s_1} c_7] k_y^2 + (c_1 + c_6 k_z) k_z \\
 & + (-1)^{s_2} \left\{ (c_3 + c_8 k_z)^2 k_y^2 + (c_4 + c_9 k_z)^2 k_z^2 \right. \\
 & \left. + [c_2 k_z + c_{10} k_y^2 + (-1)^{s_1} c_{12} k_y^2 + c_{11} k_z^2]^2 \right\}^{1/2}, \quad (3)
 \end{aligned}$$

where $s_1, s_2 \in \{0, 1\}$. The valence bands ($s_2 = 1$) are degenerate at $k_y \neq 0$, when the condition

$$c_7 \sqrt{(c_3^2 + c_4^2) k_y^2 + c_2^2 k_z^2} = c_2 c_{12} k_z \quad (4)$$

is satisfied in the leading order of k . By squaring both sides we obtain

$$c_7^2 (c_3^2 + c_4^2) k_y^2 = c_2^2 (c_{12}^2 - c_2^2) k_z^2. \quad (5)$$

Therefore, when $|c_{12}| > |c_7|$, the valence bands are degenerate along the straight lines $k_z \propto \pm k_y$ emanating from the Dirac point. Note that, according to Eq. (4), the degeneracies occur

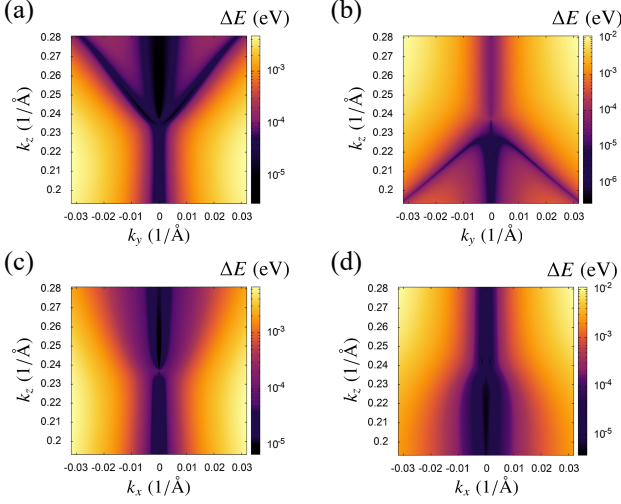


FIG. 3. Color maps of the energy difference with logarithmic scale. The energy difference between the two topmost valence bands and the two bottommost conduction bands of Y_8CoIn_3 on the mirror invariant plane $k_x = 0$ are shown in (a) and (b), respectively. The energy difference between the two topmost valence bands and between the two bottommost conduction bands on the glide invariant plane $k_y = 0$ are shown in (c) and (d), respectively.

only in the part of the lines described by Eq. (5) that satisfies $c_2c_7c_{12}k_z > 0$. Similarly, when $|c_{12}| > |c_7|$, the conduction bands are degenerate in the part of the lines represented by Eq. (5) that satisfies $c_2c_7c_{12}k_z < 0$. On the other hand, when $|c_7| > |c_{12}|$, the valence bands and the conduction bands on the $k_y = 0$ plane are degenerate in the part of the lines represented by

$$c_{12}^2(c_3^2 + c_4^2)k_x^2 = c_2^2(c_7^2 - c_{12}^2)k_z^2 \quad (6)$$

that satisfies $c_2c_7c_{12}k_z > 0$ and $c_2c_7c_{12}k_z < 0$, respectively. We note that $0 < c_2 < c_7 < c_{12}$ in Y_8CoIn_3 . From the above discussion, we conclude that in the spinless Dirac semimetal phase protected by C_{6v} symmetry, both the valence bands and the conduction bands are degenerate along the straight lines passing through the Dirac point extending to the opposite directions to each other on one of the two equivalent mirror invariant planes determined by the relative magnitude of c_7 and c_{12} .

B. Surface states

We calculate the surface states for the (1000) surface of Y_8CoIn_3 , using the surface termination shown in Fig. 4(a) and the surface BZ shown in Fig 2(b). As shown in Fig. 4(b), two nontrivial surface bands emerge from the projection of the bulk Dirac point. The absence or presence of the nontrivial surface bands in the $\bar{\Gamma}$ - \bar{Z} line corresponds to the Zak phase values of 0 or π , respectively. Also, the number of nontrivial surface bands corresponds to the number of glide sectors for which the Zak phase is π . This correspondence between the

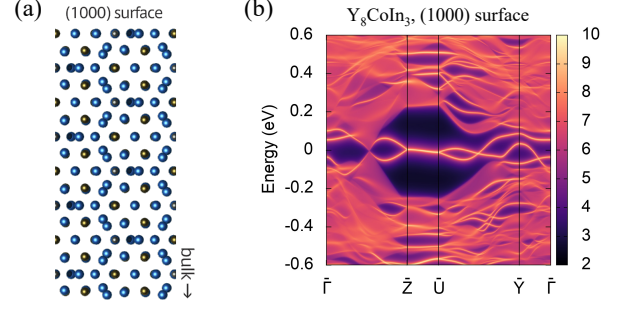


FIG. 4. Surface states in Y_8CoIn_3 . (a) The surface termination used in the calculation. (b) The surface states for the (1000) surface.

Zak phases for each sector and the nontrivial surface bands is reproduced by the 4×4 tight-binding model with the C_{6v} point group symmetry and time reversal symmetry, as described in Appendix D.

The crystal maintains the glide symmetry with respect to the zx plane when the surface is in this direction. The \bar{Z} - \bar{U} line is invariant up to the reciprocal lattice vector under the product of the glide operation $\{M_y|00\frac{1}{2}\}$ and the time reversal operation Θ . The product $\{M_y|00\frac{1}{2}\}\Theta$ is an anti-unitary operator and $(\{M_y|00\frac{1}{2}\}\Theta)^2$ is -1 when $ck_z = \pi$; therefore the Kramers-like degeneracy occurs on the \bar{Z} - \bar{U} line. This explains the degeneracy of the two midgap surface states along the \bar{Z} - \bar{U} line.

C. Topological transitions

The spinless Dirac semimetallic phases are located at the phase boundaries of various topological phases. By applying uniaxial pressure to Y_8CoIn_3 , we can transform it into a multi-band nodal-line or Weyl semimetallic phases characterized by the second SW class. Additionally, the use of lanthanides as substitutes can introduce magnetism and strong SOC since Y_8CoIn_3 mainly consists of Y.

1. The second Stiefel-Whitney class

In the space group $P6_3mc$, the $k_z = 0$ plane is invariant under the product of the twofold screw operation $\{C_{2z}|00\frac{1}{2}\}$ and the time reversal operation Θ . Since $\{C_{2z}|00\frac{1}{2}\}\Theta$ is an anti-unitary operator and satisfies $(\{C_{2z}|00\frac{1}{2}\}\Theta)^2 = +1$ in the $k_z = 0$ plane, we can adopt the real gauge for the wavefunctions in the $k_z = 0$ plane. Recalling that Y_8CoIn_3 has a finite energy gap throughout the $k_z = 0$ plane, the Hamiltonian on this plane is topologically characterized by a \mathbb{Z}_2 invariant called the second SW class [35–40]. The second SW class w_2 can be obtained by the Wilson loop method [39–42]. Figure 5(a) shows the Wilson loop spectrum of Y_8CoIn_3 calculated in the $k_z = 0$ plane, where the integral path of the Wilson loop is along the k_x direction at fixed k_y . The spectrum has one linear crossing at π , indicating $w_2 = 1$ in this plane. On the other hand, in the

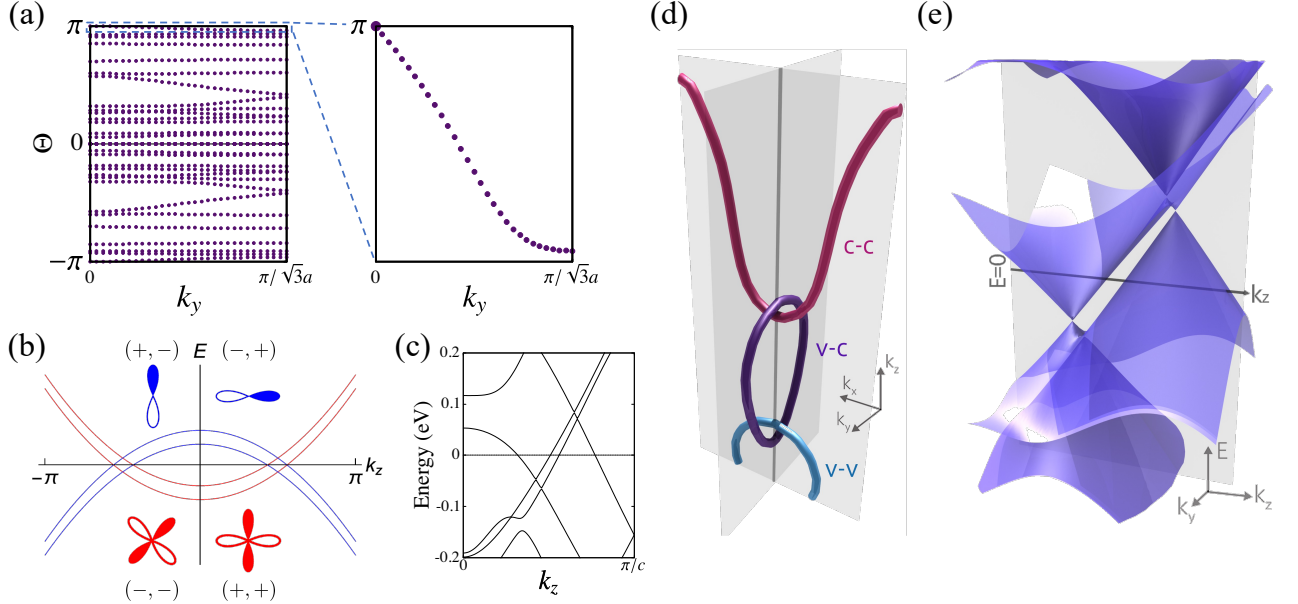


FIG. 5. The second SW class and the topological phase transitions of Y_8CoIn_3 . (a) The Wilson loop spectrum of Y_8CoIn_3 calculated in the $k_z = 0$ plane. The integral path of the Wilson loop is along the k_x direction at fixed k_y . (b) Schematic band structure of C_{2z} and Θ symmetric systems with different second SW classes in the $k_z = 0$ and $k_z = \pi$ planes. The colors of the bands, red and blue, correspond to the C_{2z} eigenvalue values, + and -, respectively. The atomic orbital-like bases and their mirror eigenvalues (eigenvalues for M_x and for M_y in this order) are also written for the case of C_{2v} symmetry. In this case, the degeneracies between a red band and a blue band occur on either the $k_x = 0$ plane or the $k_y = 0$ plane. (c) The band structure on the k_z axis of Y_8CoIn_3 compressed by 5% in the x direction. (d) The nodal structure of Y_8CoIn_3 compressed by 5% in the x direction. The nodal line between the valence and conduction bands is drawn in purple, and the nodal line between the two highest valence bands (lowest conduction bands) is drawn in blue (red). The gray planes represent the $k_x = 0$ and $k_y = 0$ planes. (e) The 3-dimensional band structure in the $k_x = 0$ plane of Y_8CoIn_3 compressed by 5% in the direction making an angle of $\pi/4$ from the x axis. The gray plane shows the k_z - E plane at $k_y = 0$.

$k_z = \pi/c$ plane, $(\{C_{2z}|00\frac{1}{2}\}\Theta)^2$ is -1 instead of $+1$. In this case, the second homotopy group of the corresponding classifying space is the trivial group and gapped Hamiltonians have no topological distinction [35].

In fact, when the system has both C_{2z} (or screw) and Θ symmetries, w_2 can be determined from the C_{2z} eigenvalues as follows [36, 39]:

$$(-1)^{w_2} = \prod_{i=1}^4 (-1)^{\lfloor N_{occ}^-(\Gamma_i)/2 \rfloor}, \quad (7)$$

where $\{\Gamma_i\}$ are the C_{2z} invariant points on the plane where w_2 is evaluated, $N_{occ}^-(\Gamma_i)$ is the number of occupied bands with negative C_{2z} eigenvalues at Γ_i , and $\lfloor \cdot \rfloor$ represents the floor function. From this formula, it can be seen that for symmorphic systems with C_{2z} and Θ symmetries, when the w_2 indices in the $k_z = 0$ and $k_z = \pi$ planes are different, two band inversions occur between bands with different C_{2z} eigenvalues as shown in Fig. 5(b), which is called a double band inversion. In this case, four bands form a gap-closing object in $0 < k_z < \pi$, which mediates the two planes with different w_2 . In Y_8CoIn_3 , the two 2-dimensional irreps Δ_5 and Δ_6 , which are distinguished by the twofold screw eigenvalues, intersect on the k_z axis, similarly to the band structure in Fig. 5(b). Although w_2 cannot be defined on the $k_z = \pi$ plane in Y_8CoIn_3 , the Dirac point can be considered to act as an intermediary

between the $k_z = 0$ plane hosting the nontrivial w_2 and the $k_z = \pi$ plane having the trivial topology.

The C_{6v} symmetry is actually not required for the definition of w_2 and its calculation from the C_{2z} eigenvalues. We thus investigate the topological phase transitions of Y_8CoIn_3 under uniaxial strains that break C_{6v} symmetry but maintain C_2 symmetry. Compressing the Y_8CoIn_3 lattice by 5% in the x direction results in space group $Cmc2_1$ (No. 36), and its little co-group on the k_z axis is C_{2v} . Figure 5(c) shows the band structure calculated on the k_z axis, where the 2-dimensional irreps are split due to the symmetry reduction. Since the twofold screw eigenvalues of the occupied bands in the $k_z = 0$ plane remain unchanged, w_2 is invariant. However, in this system, a nodal line on the mirror invariant plane $k_x = 0$ mediates the $k_z = 0$ and $k_z = \pi$ planes instead of the Dirac point. Furthermore, in this system, nodal lines between the two highest valence bands and between the two lowest conduction bands lie on the glide invariant plane $k_y = 0$ and pass inside the nodal line between the valence and conduction bands as shown in Fig. 5(d). The fact that the nodal lines appear on the two different mirror-invariant planes can be understood from the symmetry of the bands. For example, a band with the d_{xy} orbital symmetry can intersect a band with the p_x orbital symmetry in the $k_y = 0$ plane, whereas it can intersect a band with the p_y orbital symmetry in the $k_x = 0$ plane [see Fig. 5(b)]. Notably, wavefunctions with positive (negative) C_2 eigenval-

ues have the same (different) eigenvalues for the two orthogonal mirror reflections.

We analyze this system using the $k \cdot p$ Hamiltonian in Eq. (2). The k -independent perturbation that breaks C_{6v} but preserves C_{2v} symmetry has the form $c_{13}\Gamma_{0,3} + c_{14}\Gamma_{3,3}$. In the following, we investigate the nodal lines near $\mathbf{k} = \mathbf{0}$ in the leading order of k , assuming that the perturbation is sufficiently small. First, let $c_{13} = 0$ for simplicity. Then, the eigenvalues on the $k_x = 0$ plane are

$$E(0, k_y, k_z) = -(-1)^{s_1} c_{14} + [c_5 + (-1)^{s_1} c_7] k_y^2 + (c_1 + c_6 k_z) k_z + (-1)^{s_2} \left\{ (c_3 + c_8 k_z)^2 k_y^2 + (c_4 + c_9 k_z)^2 k_z^2 + [c_2 k_z + c_{10} k_y^2 + (-1)^{s_1} c_{12} k_y^2 + c_{11} k_z^2]^2 \right\}^{1/2}, \quad (8)$$

where $s_1, s_2 \in \{0, 1\}$, and the top valence and bottom conduction bands are degenerate along the curve defined by

$$(c_3^2 + c_4^2 + 2c_7 c_{14}) k_y^2 + c_2^2 k_z^2 = c_{14}^2. \quad (9)$$

Since the perturbation c_{14} is assumed to be small, this represents an ellipse around $\mathbf{k} = \mathbf{0}$. We note that this nodal ring cannot be gapped out by tuning c_{14} . Suppose we start from the nodal-line semimetal phase and change c_{14} through 0. As c_{14} approaches 0, the size of the nodal ring decreases. At $c_{14} = 0$ the nodal ring shrinks to the Dirac point, but when c_{14} becomes finite after the sign reversal, it grows into a nodal ring again.

Similarly, on the $k_y = 0$ plane, the two valence bands and also the two conduction bands are degenerate along

$$[c_{10} \pm \text{sgn}(c_{14}) c_{12}] k_x^2 + c_2 k_z = 0, \quad (10)$$

where \pm corresponds to the valence and conduction bands, respectively, and $\text{sgn}(\cdot)$ denotes the sign function. The degenerate \mathbf{k} points form two parabolas with the vertex at $\mathbf{k} = \mathbf{0}$ and thread the nodal line defined by Eq. (9). These features coincide with those of nodal lines with \mathbb{Z}_2 monopole charge in PT -symmetric systems [39, 43], where PT is the product of space inversion and time reversal operators. However, it should be noted that our system does not have space inversion symmetry, but has C_{2v} symmetry instead. In the general case with $c_{13} \neq 0$, the planes where the nodal lines emerge switch between the $k_x = 0$ and $k_y = 0$ planes depending on the relative magnitude of c_{13} and c_{14} , and the two connected parabolas of Eq. (10) are turned into two branches of a hyperbola as shown in Fig. 5(d). The details of the calculations are presented in Appendix E. Note that, depending on the sign of the perturbation parameters, the degeneracies between the valence bands and between the conduction bands represented by Eq. (5) and Eq. (6) can remain in the plane, but shift enough from the k_z axis to move outside of the nodal ring in Eq. (9).

When the system is compressed in the direction with an angle of $\pi/4$ from the x axis, the space group transforms into $P2_1$ (No. 4), and its little co-group on the k_z axis becomes C_2 . Under this distortion, the $k_z = 0$ plane still preserves the nontrivial w_2 . However, the gap-closing object bridging the

$k_z = 0$ and $k_z = \pi$ planes becomes a pair of Weyl points with opposite chirality [Fig. 5(e)]. This phenomenon is typical of Dirac semimetal phases with broken spatial inversion symmetry and has been discussed in previous studies [44–47]. The analytical argument with the $k \cdot p$ Hamiltonian is given in the Appendix F.

The results of the second SW class for the Dirac, nodal-line, and Weyl semimetals are combined as follows. The gapped Hamiltonian in the $k_z = 0$ plane of nonsymmorphic systems with $\{C_{2z}|00\frac{1}{2}\}$ and Θ is characterized by the second SW class w_2 , which takes the \mathbb{Z}_2 values. If $w_2 = 1$ and the system has a finite energy gap except on the k_z axis, a gap-closing object is formed by four bands on the k_z axis. Depending on the symmetry, it can be a pair of Weyl points, a nodal line, or a Dirac point. This is also the case for symmorphic systems with different w_2 on the $k_z = 0$ and $k_z = \pi$ planes. In this perspective, the Dirac semimetal such as $Y_8\text{CoIn}_3$ can be understood as a system with a double band inversion where the parameters are fine-tuned by the symmetry.

2. Spinful Dirac semimetal

Figure 6(a) shows the electronic band structure of Lu_8CoGa_3 calculated in the presence and absence of the SOC. The Lu $5d$ orbitals have a strong SOC compared to the Y $4d$ orbitals, resulting in the significant SOC splitting near the Fermi level in Lu_8CoGa_3 . In Fig. 6(b), the single-valued representations Δ_5 and Δ_6 transform into $\Delta_7 \oplus \Delta_9$ and $\Delta_7 \oplus \Delta_8$, respectively, when the SOC is turned on. The double-valued representations Δ_7 , Δ_8 and Δ_9 are all 2-dimensional irreps that are distinguished by the screw symmetry around the z axis. The two bands belonging to Δ_7 hybridize and open the energy gap. The hybridization of bands belonging to different representations is prohibited; therefore, three Dirac points are formed near the Fermi level, which are not related by any symmetry and have different energies. The SOC gap of Lu_8CoGa_3 can be measured by taking the energy difference between the maximum of the lower Δ_7 band and the intersection of the Δ_8 and Δ_9 bands, which approximately equals 75 meV. When Lu is replaced with Y, the magnitude of the SOC is drastically reduced to 1/3 or less (see Appendix B).

3. Magnetic Weyl semimetal

In the presence of magnetic rare-earth atoms, the time-reversal symmetry is broken. It is intriguing to examine the evolution of topological features near the Fermi energy in the presence of a finite magnetization. The Dirac cone is expected to split into a pair of Weyl points with opposing chiralities [1, 9, 14]. We have opted for Nd_8CoGa_3 as our magnetic prototype system, applying an all-electron full-potential Korringa-Kohn-Rostoker (KKR) Green function method with the GGA for exchange-correlation energy [48]. The non-magnetic La_8CoGa_3 has a small Fermi surface around the $k_z = 0$ plane (see Appendix B), and there is also a low DOS at the Fermi level when Nd replaces La [Fig. 7(a)]. The Nd

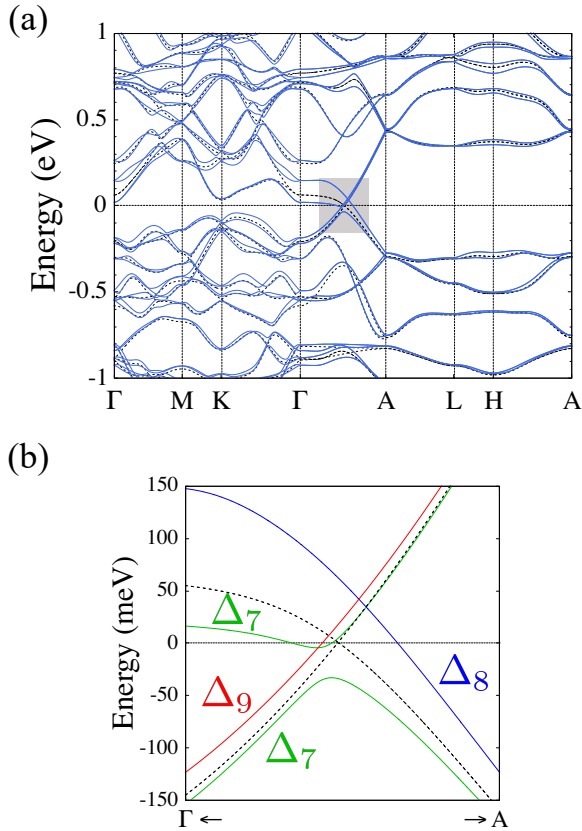


FIG. 6. The electronic band structure of Lu_8CoGa_3 calculated with and without the SOC. (a) The electronic band structure of Lu_8CoGa_3 calculated by the GGA. The blue solid line and the black dashed line show the result with and without the SOC, respectively. The energy is measured from the Fermi level in the spinless calculation. (b) Magnified band structure in the shaded region in (a). The irreps of the bands with the SOC are indicated.

magnetic atom is in a $3+$ state, and has a magnetic moment of $3.19\mu_B$ per atom in agreement with Hund's rules (the moment points along the c -axis). Due to the finite spin polarization on Nd, an induced moment of $0.43\mu_B$ emerges on the Co atoms with an antiferromagnetic coupling to the Nd atoms. Additionally, a weak induced moment of $0.04\mu_B$ appears on the Ga atoms.

The electronic band structure for Nd_8CoGa_3 without the SOC is shown in Fig. 7(b). As expected from the density of states, the gap is populated by the Co $3d$ and Ga $4p$ bands, as a consequence of the spin splitting introduced by the Nd magnetic moment [see Fig. 7(a)]. Nonetheless, the gap remains open and unaltered along the $[AL, LH, HA]$ directions. This is because a large energy gap is opened around the $k_z = \pi$ plane in $RE_8\text{CoX}_3$ materials, and the number of occupied bands in the magnetic state, excluding the $4f$ orbitals, is unchanged compared to the nonmagnetic state. Each of the Dirac points in the Γ -A line splits into a pair of Weyl points in the presence of the SOC as shown in Fig. 7(c). Furthermore, given that the filling of the gap originates from the induced spin polarization on Co and Ga, we investigate the electronic band struc-

ture in the paramagnetic phase. To simulate the paramagnetic state, we employ the disordered local moment (DLM) approach [49], the fully magnetic disordered state is then established using the coherent potential approximation (CPA) [50]. In the disordered state, the induced moments on the Co and Ga vanish, hence fewer bands are observed in the gap in comparison with the ferromagnetic state [see Fig. 7(d)]. The magnetic disorder causes the smearing of the electronic bands. The dependence of bands populating the gap on the induced spin polarization indicates that the Fermi surface, and semimetallic character can be tuned via the magnetic order and finite temperature effects. Lastly, as the magnetic order alters the topological band structure of Nd_8CoGa_3 , we performed a preliminary analysis of the magnetic interactions in real space using the infinitesimal rotation method [51], and find that the intralayer and interlayer magnetic coupling is predominantly ferromagnetic with a transition temperature of $T_c = 40$ K. The relatively high temperature can be attributed to the high number of rare-earth atoms within the unit cell.

III. CONCLUSION

In summary, the ternary compounds $RE_8\text{CoX}_3$ (RE = rare earth elements, X = Al, Ga, or In) are the ideal platform of the spinless Dirac semimetal and the topological transitions. The strength of the SOC in these materials can be adjusted by substituting elements, and those containing Y have a smaller SOC. The Dirac points in these materials are manifested by accidental degeneracy of the two different 2-dimensional irreps of C_{6v} , on the k_z axis. The degeneracies between the valence bands and between the conduction bands are generally lifted away from the k_z axis, but there are degenerate lines on the mirror planes extending from the Dirac points. The non-trivial topology of the bulk states is characterized by the Zak phases for each glide sector, which corresponds to the two midgap bands in the surface extending from the projection of the bulk Dirac point. Furthermore, we discuss the topological phase transitions under the distortions and the elemental substitutions. Uniaxial compression, which preserves the twofold screw symmetry, breaks the C_{6v} symmetry and turns the Dirac point into the nodal line or the pair of Weyl points. The magnetic lanthanide elements can replace Y, resulting in a spinful magnetic Weyl semimetallic phase in the system.

ACKNOWLEDGMENTS

The authors thank S. Murakami for the valuable discussions. This work was supported by JST CREST (Grant No. JPMJCR19T2). S.S. acknowledges financial support from JSPS KAKENHI Grants No. 23K13056 and No. 23K03333. S.K. acknowledges financial support from JSPS KAKENHI Grants No. 19K14612 and No. 22K03478. M.H. acknowledges financial support from PRESTO, JST (JPMJPR21Q6) and JSPS KAKENHI Grants No. 18H03678.

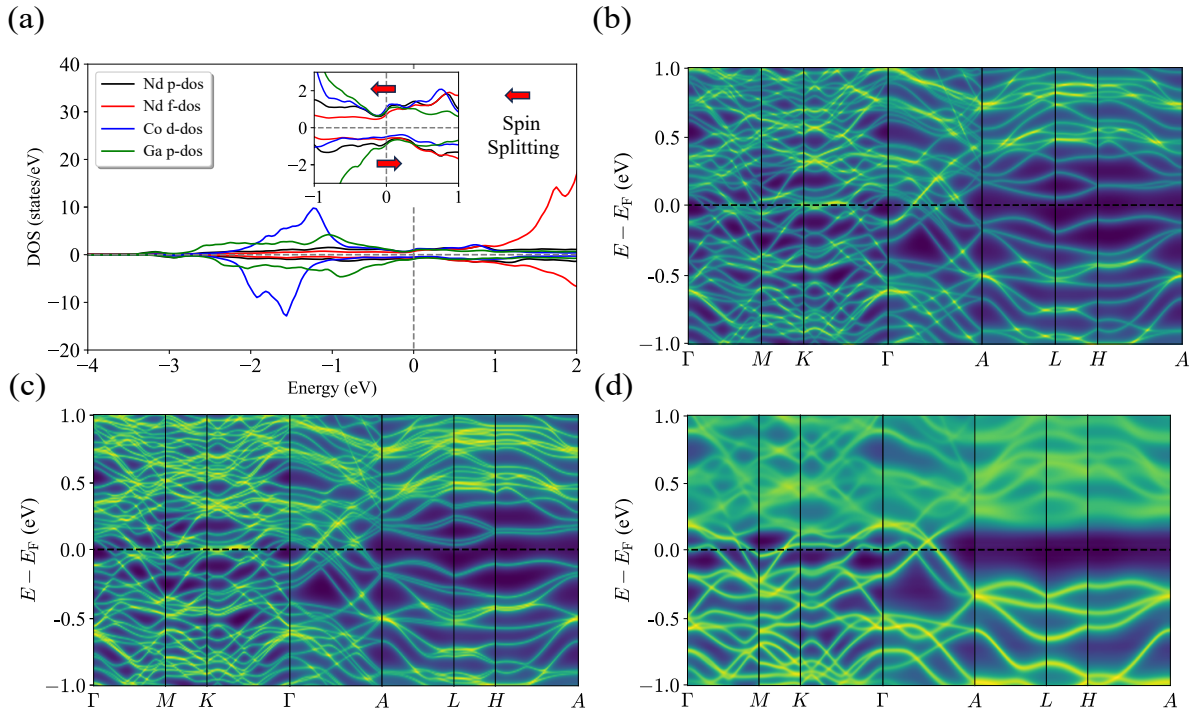


FIG. 7. The electronic structure of the magnetic material Nd_8CoGa_3 calculated by the KKR method. (a) The PDOS of Nd_8CoGa_3 calculated without the SOC. The inset is a magnified figure near the Fermi level showing the spin splitting of the Co and Ga atoms. (b) The electronic band structure of Nd_8CoGa_3 without the SOC. (c) The electronic band structure of Nd_8CoGa_3 with the SOC included self-consistently in ferromagnetic configurations. (d) The electronic band structure of Nd_8CoGa_3 in the paramagnetic state computed using the DLM approach. The smearing of the bands is due to the finite temperature effects.

Appendix A: METHOD

The electronic structure of Y_8CoIn_3 is calculated based on density functional theory (DFT) as implemented in the Vienna Ab initio Simulation Package (VASP) [52]. For the exchange-correlation functional, we employ the GGA of Perdew, Burke, and Ernzerhof (PBE) [53]. The cutoff energy for the plane wave expansion is 350 eV and a k -point mesh of $8 \times 8 \times 12$ is adopted. The calculations are based on the experimental crystal structure. To calculate the PDOS, Zak phases, and surface states, we construct a tight-binding Hamiltonian from the DFT results using the Wannier90 package [54]. From the Bloch functions within the range from 4 eV below to 10 eV above the Fermi level, we construct 114 Wannier functions for the Y $4d$ orbitals, the Co $3d$ orbitals, the In $5p$ orbitals, and the interstitial s orbitals near the Co atoms. The surface states are calculated by the iterative Green's function method [55–57] implemented in the WannierTools package [58]. The WannierTools package is also used, *mutatis mutandis*, to calculate the Zak phases. When we investigate topological phase transitions caused by uniaxial strains, the lattice is compressed in one direction and expanded uniformly in the two orthogonal directions so that the volume of the unit cell is preserved, and then the structure is optimized using the revised PBE for solids (PBEsol) [59] as the exchange-correlation functional.

For the magnetic Weyl semimetals our first-principles sim-

ulations employ the all-electron full-potential KKR Green function method [60] with and without SOC. The $4f$ electrons are treated using the DFT+ U approach in the Dudarev formulation [61] with $U = 6$ eV. The self-consistent energy contour is divided into 48 energy points with a $25 \times 25 \times 25$ k -mesh in the BZ. The electronic band structure along the high symmetry path represents the quasiparticle density of states (QDOS) computed directly from Green function in the ordered ferromagnetic or paramagnetic (DLM) states [62].

Appendix B: Band structures of other materials in $RE_8\text{CoX}_3$

In this section, we discuss the band structures of nonmagnetic materials in $RE_8\text{CoX}_3$: $RE_8\text{CoX}_3$ with $RE = \{\text{Y, La, Lu}\}$ and $X = \{\text{Al, Ga, In}\}$ other than Lu_8CoGa_3 . In the calculations, the experimental crystal structure is used for Lu_8CoIn_3 [32], while for the other materials the crystal structures are optimized using the PBEsol in the GGA as the exchange-correlation functional. The other calculation conditions are the same as for the Y_8CoIn_3 calculation. Figure 8 shows the band structures calculated in the presence and absence of the SOC. Y_8CoAl_3 , Y_8CoGa_3 and Y_8CoIn_3 are ideal spinless Dirac semimetals, while the other materials have extra Fermi surfaces. The SOC gaps of Y_8CoX_3 ($X = \text{Al, Ga, In}$), measured in the same way as Lu_8CoGa_3 in the main text, are

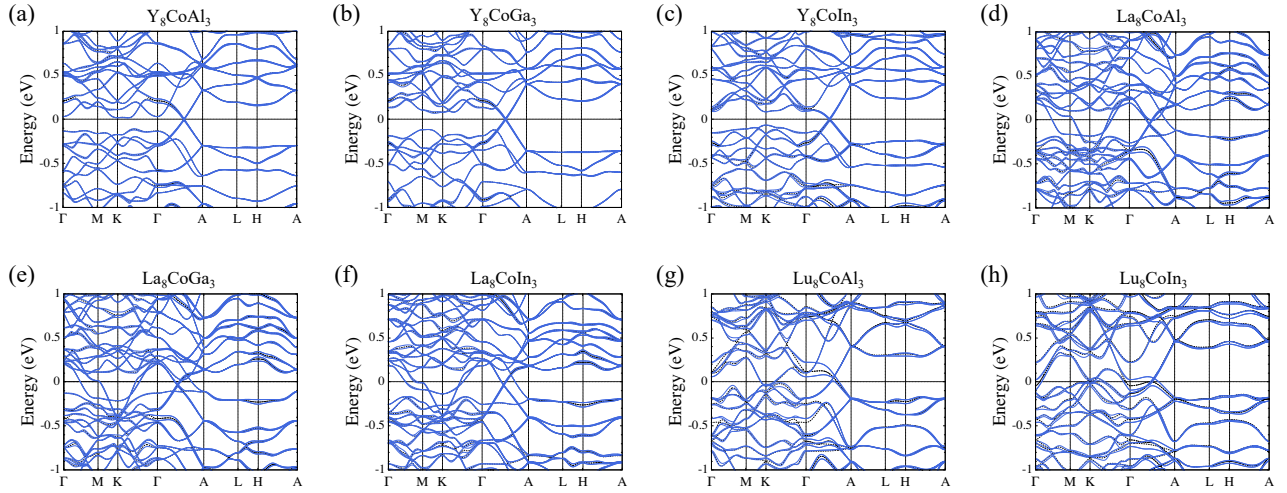


FIG. 8. The electronic band structures of RE_8CoX_3 with $RE = \{Y, La, Lu\}$ and $X = \{Al, Ga, In\}$ other than Lu_8CoGa_3 , calculated with and without the SOC. The blue solid line and the black dashed line show the result with and without the SOC, respectively. The energy is measured from the Fermi level. (a) Y_8CoAl_3 . (b) Y_8CoGa_3 . (c) Y_8CoIn_3 . (d) La_8CoAl_3 . (e) La_8CoGa_3 . (f) La_8CoIn_3 . (g) Lu_8CoAl_3 . (h) Lu_8CoIn_3 .

TABLE I. The fitted parameters for the Hamiltonian in Eq.(2).

c_1	c_2	c_3	c_4
0.230 eV Å	1.39 eV Å	1.15 eV Å	1.15 eV Å
c_5	c_6	c_7	c_8
$-0.732 \text{ eV} \text{ \AA}^2$	$-0.136 \text{ eV} \text{ \AA}^2$	$1.93 \text{ eV} \text{ \AA}^2$	$-1.91 \text{ eV} \text{ \AA}^2$
c_9	c_{10}	c_{11}	c_{12}
$0.615 \text{ eV} \text{ \AA}^2$	$0 \text{ eV} \text{ \AA}^2$	$1.93 \text{ eV} \text{ \AA}^2$	$2.65 \text{ eV} \text{ \AA}^2$

21 meV, 20 meV, and 28 meV, respectively.

Appendix C: parameters of the $k \cdot p$ Hamiltonian

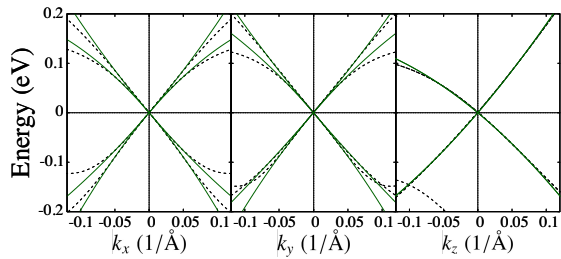


FIG. 9. The comparison of the band structure of Y_8CoIn_3 near the Dirac point between the $k \cdot p$ model in Eq. (2) and the first-principles calculations. The green solid line and the black dashed line represent the band structure of the $k \cdot p$ Hamiltonian with the parameters in Table I and the first-principles calculations, respectively.

Table I shows the fitted parameters of the Hamiltonian in Eq. (2). These parameters reproduce well the band structure of the first-principles calculation in the vicinity of the Dirac point, as shown in Fig. 9.

Appendix D: Tight-binding model

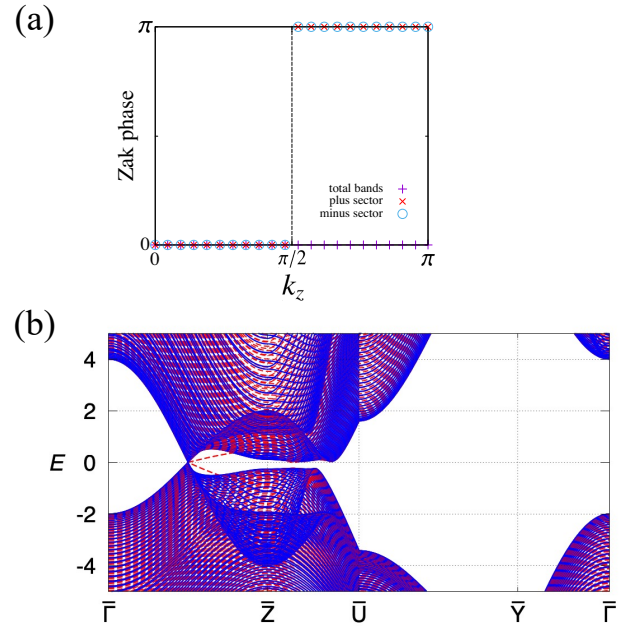


FIG. 10. The Zak phases and surface states of the tight-binding Hamiltonian in Eq. (D1), where the parameters are chosen as $(c_1, c_2, c_3, c_4, c_5, c_6, c_7, c_8, c_9, c_{10}, c_{11}, c_{12}) = (0, 0, 1, 0, 1, 1, 1, 0, 1, 3, 3, 1)$. (a) The Zak phases along the x axis for each glide sector. The dashed line represents the coordinate of the Dirac point ($k_z = \pi/2$). (b) The energy band structure calculated with a slab consisting of 128 unit cells along the x -axis. The blue solid and red dashed lines represent the band structure calculated under the periodic and open boundary conditions, respectively.

Here we present a tight-binding model on a hexagonal lat-

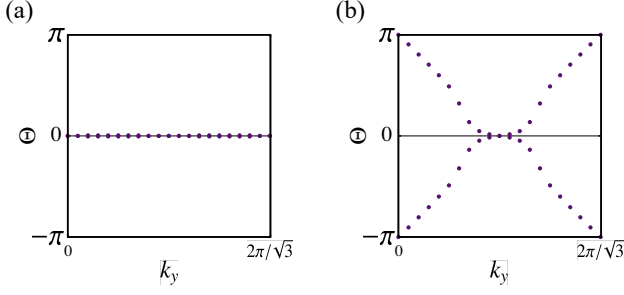


FIG. 11. The Wilson loop spectra of the tight-binding Hamiltonian in Eq. (D1) for (a) $k_z = 0$ and (b) $k_z = \pi$ planes, where we choose the same parameters as in Fig. 10. The integral path of the Wilson loop is along the k_x direction at fixed k_y .

tice with C_{6v} symmetry and discuss some topological properties. The lattice Hamiltonian has the form

$$\begin{aligned}
 H_{\text{lat}}(\mathbf{k}) = & c_1 \sin k_z \Gamma_{0,0} + c_2 \sin k_z \Gamma_{3,0} \\
 & + (c_3 + c_8 \sin k_z)[e_{11}(\mathbf{k})\Gamma_{2,0} - e_{12}(\mathbf{k})\Gamma_{1,2}] \\
 & + (c_4 + c_9 \sin k_z)[e_{11}(\mathbf{k})\Gamma_{1,0} + e_{12}(\mathbf{k})\Gamma_{2,2}] \\
 & + c_5 a_1(\mathbf{k})\Gamma_{0,0} + c_6 \cos k_z \Gamma_{0,0} \\
 & + c_7 [e_{21}(\mathbf{k})\Gamma_{3,3} - e_{22}(\mathbf{k})\Gamma_{0,1}] \\
 & + c_{10} a_1(\mathbf{k})\Gamma_{3,0} + c_{11} \cos k_z \Gamma_{3,0} \\
 & + c_{12} [e_{21}(\mathbf{k})\Gamma_{0,3} - e_{22}(\mathbf{k})\Gamma_{3,1}], \quad (\text{D1})
 \end{aligned}$$

where

$$\begin{aligned}
 a_1(\mathbf{k}) = & 4 - \frac{4}{3} \left(\cos k_x + \cos \frac{-k_x + \sqrt{3}k_y}{2} \right. \\
 & \left. + \cos \frac{-k_x - \sqrt{3}k_y}{2} \right), \quad (\text{D2})
 \end{aligned}$$

$$e_{11}(\mathbf{k}) = \frac{2}{3} \left(2 \cos \frac{k_x}{2} + \cos \frac{\sqrt{3}k_y}{2} \right) \sin \frac{k_x}{2}, \quad (\text{D3})$$

$$e_{12}(\mathbf{k}) = \frac{2\sqrt{3}}{3} \cos \frac{k_x}{2} \sin \frac{\sqrt{3}k_y}{2}, \quad (\text{D4})$$

$$e_{21}(\mathbf{k}) = -\frac{8}{3} \left(\cos k_x - \cos \frac{k_x}{2} \cos \frac{\sqrt{3}k_y}{2} \right), \quad (\text{D5})$$

$$e_{22}(\mathbf{k}) = \frac{8\sqrt{3}}{3} \sin \frac{k_x}{2} \sin \frac{\sqrt{3}k_y}{2}. \quad (\text{D6})$$

This Hamiltonian is identical to the $k \cdot p$ Hamiltonian in Eq. (2) up to the second order in k . Note that $\mathbf{k} = \mathbf{0}$ is the Γ point in this lattice model, whereas it represents the position of the Dirac point in the $k \cdot p$ Hamiltonian. Therefore, the tight-binding Hamiltonian (D1) has to satisfy the time reversal symmetry $\Theta = \Gamma_{0,0}K$ (K : complex conjugation), which results in $c_1 = c_2 = c_4 = c_8 = 0$. In these constraints, Dirac points are located at $(0, 0, \pm\pi/2)$.

Figure 10(a) shows the Zak phase for each glide sector, where the integration is performed along the k_x axis in the $k_y = 0$ plane. As is the case in Y_8CoIn_3 , the Zak phases in both sectors change by π at the Dirac point. To confirm the

correspondence between the Zak phases and the surface states, we perform the Fourier transformation of the Hamiltonian in Eq. (D1) with respect to the k_x direction, and calculate the energy eigenvalues under the periodic and open boundary conditions. As seen in Fig. 10(b), in the open boundary condition, the two surface bands extend from the Dirac point towards the \bar{Z} point, corresponding to the nontrivial Zak phases.

Since this model has the pure rotational symmetry rather than the screw, the $C_{2z}\Theta$ -symmetry-protected topological number can be defined not only in the $k_z = 0$ plane but also in the $k_z = \pi$ plane. The number of the occupied bands in this model is two, and thus the topological number is given by the \mathbb{Z} -valued Euler class [36–38]. Figure 11 shows the Wilson loop spectra calculated in the $k_z = 0$ and $k_z = \pi$ planes, where the integral path of the Wilson loop is along the k_x direction at fixed k_y . As shown by Fig. 11(a), the Wilson loop spectrum in the $k_z = 0$ plane shows no windings, which indicates the trivial (zero) Euler class. On the other hand, Fig. 11(b) shows the Wilson loop spectrum with the winding number $+1$ and -1 , which implies that the Euler class is 1, in the $k_z = \pi$ plane. Therefore, the Dirac point in this system can be considered to emerge as a gap-closing object bridging the two planes with the different Euler classes.

Appendix E: $k \cdot p$ Hamiltonian with C_{2v} symmetry

In this Appendix, we discuss the nodal lines near $\mathbf{k} = \mathbf{0}$ analytically for the Hamiltonian in Eq. (2) with the perturbation $c_{13}\Gamma_{0,3} + c_{14}\Gamma_{3,3}$, which reduces the symmetry to C_{2v} . In the following, we assume that the perturbation is sufficiently small and that $|c_{13}| \neq |c_{14}|$. In the following, we assume that the perturbation is sufficiently small and that $|c_{13}| \neq |c_{14}|$.

The eigenvalues on the $k_x = 0$ plane are

$$\begin{aligned}
 E(0, k_y, k_z) = & (-1)^{s_1} c_{14} + (c_5 - (-1)^{s_1} c_7) k_y^2 + (c_1 + c_6 k_z) k_z \\
 & + (-1)^{s_2} \left\{ (c_3 + c_8 k_z)^2 k_y^2 + (c_4 + c_9 k_z)^2 k_y^2 \right. \\
 & \left. + \left[(-1)^{s_1} c_{13} + c_2 k_z + c_{10} k_y^2 - (-1)^{s_1} c_{12} k_y^2 + c_{11} k_z^2 \right]^2 \right\}^{1/2}, \quad (\text{E1})
 \end{aligned}$$

where $s_1, s_2 \in \{0, 1\}$. When $c_{14} > 0$, the top valence and bottom conduction bands are degenerate at \mathbf{k} that satisfy

$$\begin{aligned}
 & 2(c_{14} - c_7 k_y^2) \\
 = & \left[(c_3 + c_8 k_z)^2 k_y^2 + (c_4 + c_9 k_z)^2 k_y^2 \right. \\
 & \left. + (c_{13} + c_2 k_z + c_{10} k_y^2 - c_{12} k_y^2 + c_{11} k_z^2)^2 \right]^{1/2} \\
 & + \left[(c_3 + c_8 k_z)^2 k_y^2 + (c_4 + c_9 k_z)^2 k_y^2 \right. \\
 & \left. + (-c_{13} + c_2 k_z + c_{10} k_y^2 + c_{12} k_y^2 + c_{11} k_z^2)^2 \right]^{1/2}. \quad (\text{E2})
 \end{aligned}$$

Eliminating the square roots by squaring both sides twice, we obtain

$$\begin{aligned}
 & c_{14} \left\{ c_{14}(c_3^2 + c_4^2) - 2 \left[(c_{13}^2 - 2c_{14}^2)c_7 + c_{13}c_{14}c_{12} \right] \right\} k_y^2 \\
 & + (c_{14}^2 - c_{13}^2)c_2^2 k_z^2 = c_{14}^2(c_{14}^2 - c_{13}^2) \quad (\text{E3})
 \end{aligned}$$

up to the second order in k . To make this equation equivalent to the original one, we need

$$c_{14} - c_7 k_y^2 > 0 \quad (\text{E4})$$

and

$$(c_3^2 + c_4^2 - 2c_{12}c_{13} + 4c_7c_{14})k_y^2 + c_2^2 k_z^2 < 2c_{14}^2 - c_{13}^2. \quad (\text{E5})$$

No wavevector \mathbf{k} satisfies Eq. (E5) when $2c_{14}^2 - c_{13}^2 < 0$, whereas Eq. (E5) is satisfied inside the ellipse when $2c_{14}^2 - c_{13}^2 > 0$. If $|c_{13}| > |c_{14}|$, Eq. (E3) represents a hyperbola, and this exists outside the ellipse in Eq. (E5). Conversely, if $|c_{13}| < |c_{14}|$, Eq. (E3) represents an ellipse, and this lies inside the ellipse in Eq. (E5). Recalling that we assume $c_{14} > 0$, the ellipse in Eq. (E3) also satisfies Eq. (E4) when $|c_{13}| < |c_{14}|$. A similar result holds when $c_{14} < 0$. Therefore, in the $k_x = 0$ plane, the top valence and bottom conduction bands are degenerate on the ellipse of Eq. (E3) when $|c_{13}| < |c_{14}|$.

On the other hand, the two valence bands are degenerate in the part of the curve

$$\begin{aligned} & -c_{14} \left\{ c_{14}(c_3^2 + c_4^2) - 2 \left[(c_{13}^2 - 2c_{14}^2)c_7 + c_{13}c_{14}c_{12} \right] \right\} k_y^2 \\ & + (c_{13}^2 - c_{14}^2)c_2^2 k_z^2 = c_{14}^2(c_{13}^2 - c_{14}^2) \end{aligned} \quad (\text{E6})$$

that satisfies

$$c_{13}c_{14}(c_{10}k_y^2 + c_2k_z) > 0 \quad (\text{E7})$$

and

$$(c_3^2 + c_4^2 - 2c_{12}c_{13} + 4c_7c_{14})k_y^2 + c_2^2 k_z^2 > 2c_{14}^2 - c_{13}^2. \quad (\text{E8})$$

If $|c_{13}| < |c_{14}|$, Eq. (E6) describes an ellipse, and this does not fulfill Eq. (E8). On the contrary, if $|c_{13}| > |c_{14}|$, Eq. (E6) shows a hyperbola, and this satisfies Eq. (E8). The hyperbola in Eq. (E6) consists of two curves passing through $(0, 0, \pm c_{14}/c_2)$ respectively, but according to Eq. (E7), only the one passing through $(0, 0, \text{sgn}(c_{13})c_{14}/c_2)$ becomes the nodal line. A similar calculation for the two conduction bands shows that they are degenerate on the other curve of the hyperbola when $|c_{13}| > |c_{14}|$. Note that the condition on the parameters c_{13} and c_{14} for the top valence and bottom conduction bands to be degenerate in the $k_x = 0$ plane is different from that for the valence bands and the conduction bands.

In the $k_y = 0$ plane, the top valence and bottom conduction bands are degenerate along the ellipse

$$\begin{aligned} & c_{13} \left\{ c_{13}(c_3^2 + c_4^2) + 2 \left[(c_{14}^2 - 2c_{13}^2)c_{12} + c_{13}c_{14}c_7 \right] \right\} k_x^2 \\ & + (c_{13}^2 - c_{14}^2)c_2^2 k_z^2 = c_{13}^2(c_{13}^2 - c_{14}^2) \end{aligned} \quad (\text{E9})$$

when $|c_{13}| > |c_{14}|$, while the two valence bands and the two conduction bands are degenerate along the hyperbola

$$\begin{aligned} & -c_{13} \left\{ c_{13}(c_3^2 + c_4^2) + 2 \left[(c_{14}^2 - 2c_{13}^2)c_{12} + c_{13}c_{14}c_7 \right] \right\} k_x^2 \\ & + (c_{14}^2 - c_{13}^2)c_2^2 k_z^2 = c_{13}^2(c_{14}^2 - c_{13}^2) \end{aligned} \quad (\text{E10})$$

when $|c_{13}| < |c_{14}|$.

In summary, whether $|c_{13}| < |c_{14}|$ or $|c_{13}| > |c_{14}|$, the valence and conduction bands are degenerate along the ellipse, while the two valence bands and the two conduction bands are degenerate along the hyperbola, which lies on the plane orthogonal to that for the ellipse and passes through the interior of the ellipse.

Appendix F: $k \cdot p$ Hamiltonian with C_2 symmetry

In this Appendix, we add $c_{13}\Gamma_{3,1} + c_{14}\Gamma_{3,2}$ to the Hamiltonian of Eq. (2) as an example of a perturbation that reduces the symmetry to C_2 , and discuss the Weyl points analytically. The eigenstates on the k_z axis are

$$|\psi_1\rangle = \frac{1}{\sqrt{2}} \begin{pmatrix} \frac{-c_{13} + ic_{14}}{\sqrt{c_{13}^2 + c_{14}^2}}, 1, 0, 0 \end{pmatrix}^T, \quad (\text{F1})$$

$$|\psi_2\rangle = \frac{1}{\sqrt{2}} \begin{pmatrix} 0, 0, \frac{-c_{13} + ic_{14}}{\sqrt{c_{13}^2 + c_{14}^2}}, 1 \end{pmatrix}^T, \quad (\text{F2})$$

$$|\psi_3\rangle = \frac{1}{\sqrt{2}} \begin{pmatrix} \frac{c_{13} - ic_{14}}{\sqrt{c_{13}^2 + c_{14}^2}}, 1, 0, 0 \end{pmatrix}^T, \quad (\text{F3})$$

$$|\psi_4\rangle = \frac{1}{\sqrt{2}} \begin{pmatrix} 0, 0, \frac{c_{13} - ic_{14}}{\sqrt{c_{13}^2 + c_{14}^2}}, 1 \end{pmatrix}^T, \quad (\text{F4})$$

where T denotes the transpose. When $c_2 > 0$, $|\psi_1\rangle$ and $|\psi_2\rangle$ are degenerate on the k_z axis at

$$k_z = k_+ := \frac{-c_2 + \sqrt{c_2^2 + 4c_{11} \sqrt{c_{13}^2 + c_{14}^2}}}{2c_{11}} > 0, \quad (\text{F5})$$

and $|\psi_3\rangle$ and $|\psi_4\rangle$ are degenerate on the k_z axis at

$$k_z = k_- := \frac{-c_2 + \sqrt{c_2^2 - 4c_{11} \sqrt{c_{13}^2 + c_{14}^2}}}{2c_{11}} < 0. \quad (\text{F6})$$

The Hamiltonian projected onto the subspace spanned by $|\psi_1\rangle$ and $|\psi_2\rangle$ is

$$H_{\text{Weyl},+}(\mathbf{k}) = \sum_{i=0}^3 f_i(\mathbf{k})\sigma_i, \quad (\text{F7})$$

where

$$f_0(\mathbf{k}) = (c_1 + c_6 k_z)k_z + \frac{2c_7 c_{13} k_x k_y}{\sqrt{c_{13}^2 + c_{14}^2}} + c_5(k_x^2 + k_y^2), \quad (\text{F8})$$

$$f_1(\mathbf{k}) = (c_4 + c_9 k_z)k_x + \frac{c_{14}(c_3 + c_8 k_z)k_y}{\sqrt{c_{13}^2 + c_{14}^2}}, \quad (\text{F9})$$

$$f_2(\mathbf{k}) = -(c_3 + c_8 k_z)k_x + \frac{c_{14}(c_4 + c_9 k_z)k_y}{\sqrt{c_{13}^2 + c_{14}^2}}, \quad (\text{F10})$$

$$\begin{aligned} f_3(\mathbf{k}) = & \sqrt{c_{13}^2 + c_{14}^2} - (c_2 + c_{11} k_z)k_z - \frac{2c_{12}c_{13}k_x k_y}{\sqrt{c_{13}^2 + c_{14}^2}} \\ & - c_{10}(k_x^2 + k_y^2). \end{aligned} \quad (\text{F11})$$

The chirality of the Weyl point is calculated as

$$\text{sgn} \left(\det \left(\frac{\partial f_i}{\partial k_j} \right) \Big|_{i,j} \Big|_{\mathbf{k}=(0,0,k_z)} \right) = -\text{sgn}(c_{14}). \quad (\text{F12})$$

By the same calculation, the chirality of the Weyl point created by $|\psi_3\rangle$ and $|\psi_4\rangle$ at $(0, 0, k_-)$ is $\text{sgn}(c_{14})$. Thus, it is shown analytically that the addition of the perturbation

$c_{13}\Gamma_{3,1} + c_{14}\Gamma_{3,2}$, which reduces the symmetry to C_2 , produces the Weyl points of opposite chirality on the k_z axis. When $c_2 < 0$, the sign of the k_z coordinate and the chirality of the Weyl points are reversed, but the above conclusion remains the same. Note that the Weyl points are generated on the k_z axis even when $c_{13} = 0$, in which case the system has C_6 symmetry.

-
- [1] N. P. Armitage, E. J. Mele, and A. Vishwanath, Weyl and Dirac semimetals in three-dimensional solids, *Rev. Mod. Phys.* **90**, 015001 (2018).
- [2] S.-Y. Xu, N. Alidoust, I. Belopolski, Z. Yuan, G. Bian, T.-R. Chang, H. Zheng, V. N. Strocov, D. S. Sanchez, G. Chang, C. Zhang, D. Mou, Y. Wu, L. Huang, C.-C. Lee, S.-M. Huang, B. Wang, A. Bansil, H.-T. Jeng, T. Neupert, A. Kaminski, H. Lin, S. Jia, and M. Zahid Hasan, Discovery of a Weyl fermion state with Fermi arcs in niobium arsenide, *Nature Physics* **11**, 748 (2015).
- [3] L. X. Yang, Z. K. Liu, Y. Sun, H. Peng, H. F. Yang, T. Zhang, B. Zhou, Y. Zhang, Y. F. Guo, M. Rahn, D. Prabhakaran, Z. Hussain, S.-K. Mo, C. Felser, B. Yan, and Y. L. Chen, Weyl semimetal phase in the non-centrosymmetric compound TaAs, *Nature Physics* **11**, 728 (2015).
- [4] B. Q. Lv, H. M. Weng, B. B. Fu, X. P. Wang, H. Miao, J. Ma, P. Richard, X. C. Huang, L. X. Zhao, G. F. Chen, Z. Fang, X. Dai, T. Qian, and H. Ding, Experimental Discovery of Weyl Semimetal TaAs, *Phys. Rev. X* **5**, 031013 (2015).
- [5] H. Weng, C. Fang, Z. Fang, B. A. Bernevig, and X. Dai, Weyl Semimetal Phase in Noncentrosymmetric Transition-Metal Monophosphides, *Phys. Rev. X* **5**, 011029 (2015).
- [6] M. Hirayama, R. Okugawa, S. Ishibashi, S. Murakami, and T. Miyake, Weyl Node and Spin Texture in Trigonal Tellurium and Selenium, *Phys. Rev. Lett.* **114**, 206401 (2015).
- [7] S. M. Young, S. Zaheer, J. C. Y. Teo, C. L. Kane, E. J. Mele, and A. M. Rappe, Dirac Semimetal in Three Dimensions, *Phys. Rev. Lett.* **108**, 140405 (2012).
- [8] Z. K. Liu, B. Zhou, Y. Zhang, Z. J. Wang, H. M. Weng, D. Prabhakaran, S.-K. Mo, Z. X. Shen, Z. Fang, X. Dai, Z. Hussain, and Y. L. Chen, Discovery of a Three-Dimensional Topological Dirac Semimetal, Na_3Bi , *Science* **343**, 864 (2014), <https://www.science.org/doi/pdf/10.1126/science.1245085>.
- [9] Z. Wang, Y. Sun, X.-Q. Chen, C. Franchini, G. Xu, H. Weng, X. Dai, and Z. Fang, Dirac semimetal and topological phase transitions in A_3Bi ($\text{A} = \text{Na}, \text{K}, \text{Rb}$), *Phys. Rev. B* **85**, 195320 (2012).
- [10] M. Neupane, S.-Y. Xu, R. Sankar, N. Alidoust, G. Bian, C. Liu, I. Belopolski, T.-R. Chang, H.-T. Jeng, H. Lin, A. Bansil, F. Chou, and M. Z. Hasan, Observation of a three-dimensional topological Dirac semimetal phase in high-mobility Cd_3As_2 , *Nature Communications* **5**, 3786 (2014).
- [11] Z. K. Liu, J. Jiang, B. Zhou, Z. J. Wang, Y. Zhang, H. M. Weng, D. Prabhakaran, S.-K. Mo, H. Peng, P. Dudin, T. Kim, M. Hoesch, Z. Fang, X. Dai, Z. X. Shen, D. L. Feng, Z. Hussain, and Y. L. Chen, A stable three-dimensional topological Dirac semimetal Cd_3As_2 , *Nature Materials* **13**, 677 (2014).
- [12] S. Jeon, B. B. Zhou, A. Gyenis, B. E. Feldman, I. Kimchi, A. C. Potter, Q. D. Gibson, R. J. Cava, A. Vishwanath, and A. Yazdani, Landau quantization and quasiparticle interference in the three-dimensional Dirac semimetal Cd_3As_2 , *Nature Materials* **13**, 851 (2014).
- [13] S. Borisenko, Q. Gibson, D. Evtushinsky, V. Zabolotnyy, B. Büchner, and R. J. Cava, Experimental Realization of a Three-Dimensional Dirac Semimetal, *Phys. Rev. Lett.* **113**, 027603 (2014).
- [14] Z. Wang, H. Weng, Q. Wu, X. Dai, and Z. Fang, Three-dimensional Dirac semimetal and quantum transport in Cd_3As_2 , *Phys. Rev. B* **88**, 125427 (2013).
- [15] Y. Kim, B. J. Wieder, C. L. Kane, and A. M. Rappe, Dirac Line Nodes in Inversion-Symmetric Crystals, *Phys. Rev. Lett.* **115**, 036806 (2015).
- [16] R. Yu, H. Weng, Z. Fang, X. Dai, and X. Hu, Topological Node-Line Semimetal and Dirac Semimetal State in Antiperovskite Cu_3PdN , *Phys. Rev. Lett.* **115**, 036807 (2015).
- [17] M. Hirayama, R. Okugawa, T. Miyake, and S. Murakami, Topological Dirac nodal lines and surface charges in fcc alkaline earth metals, *Nature Communications* **8**, 14022 (2017).
- [18] H. C. Po, A. Vishwanath, and H. Watanabe, Symmetry-based indicators of band topology in the 230 space groups, *Nature Communications* **8**, 50 (2017).
- [19] B. Bradlyn, L. Elcoro, J. Cano, M. G. Vergniory, Z. Wang, C. Felser, M. I. Aroyo, and B. A. Bernevig, Topological quantum chemistry, *Nature* **547**, 298 (2017).
- [20] F. Tang, H. C. Po, A. Vishwanath, and X. Wan, Efficient topological materials discovery using symmetry indicators, *Nature Physics* **15**, 470 (2019).
- [21] T. Zhang, Y. Jiang, Z. Song, H. Huang, Y. He, Z. Fang, H. Weng, and C. Fang, Catalogue of topological electronic materials, *Nature* **566**, 475 (2019).
- [22] M. G. Vergniory, L. Elcoro, C. Felser, N. Regnault, B. A. Bernevig, and Z. Wang, A complete catalogue of high-quality topological materials, *Nature* **566**, 480 (2019).
- [23] F. Tang, H. C. Po, A. Vishwanath, and X. Wan, Topological materials discovery by large-order symmetry indicators, *Science Advances* **5**, eaau8725 (2019), <https://www.science.org/doi/pdf/10.1126/sciadv.aau8725>.
- [24] D. Wang, F. Tang, J. Ji, W. Zhang, A. Vishwanath, H. C. Po, and X. Wan, Two-dimensional topological materials discovery by symmetry-indicator method, *Phys. Rev. B* **100**, 195108 (2019).
- [25] M. G. Vergniory, B. J. Wieder, L. Elcoro, S. S. P. Parkin, C. Felser, B. A. Bernevig, and N. Regnault, All topological bands of all nonmagnetic stoichiometric materials, *Science* **376**, eabg9094 (2022), <https://www.science.org/doi/pdf/10.1126/science.abg9094>.
- [26] We note that the spin degrees of freedom are ignored when counting the degree of degeneracy.
- [27] Z. Song, T. Zhang, and C. Fang, Diagnosis for Nonmagnetic Topological Semimetals in the Absence of Spin-Orbital Coupling, *Phys. Rev. X* **8**, 031069 (2018).

- [28] B.-J. Yang and N. Nagaosa, Classification of stable three-dimensional Dirac semimetals with nontrivial topology, *Nature Communications* **5**, 4898 (2014).
- [29] B.-J. Yang, T. Morimoto, and A. Furusaki, Topological charges of three-dimensional Dirac semimetals with rotation symmetry, *Phys. Rev. B* **92**, 165120 (2015).
- [30] Z.-M. Yu, Z. Zhang, G.-B. Liu, W. Wu, X.-P. Li, R.-W. Zhang, S. A. Yang, and Y. Yao, Encyclopedia of emergent particles in three-dimensional crystals, *Science Bulletin* **67**, 375 (2022).
- [31] M. Dzevenko, A. Hamyk, Y. Tyvanchuk, and Y. Kalychak, Phase equilibria in the Er-Co-In system and crystal structure of Er₈CoIn₃ compound, *Open Chemistry* **11**, 604 (2013).
- [32] M. Dzevenko, I. Bigun, M. Pustovoychenko, L. Havela, and Y. Kalychak, Rare-earth rich indides RE₈CoIn₃ (RE = Y, Dy–Tm, Lu), *Intermetallics* **38**, 14 (2013).
- [33] Y. Grin, O. Sichevich, R. Gladyshevskii, and Y. Yarmolyuk, The crystal structure of the compounds R₈Ga₃Co (R= Ce, Pr, Nd, Sm, Tb, Dy, Ho, Er, Tm), *Kristallografiya* **29**, 708 (1984).
- [34] M. G. Kibria and M. R. Shattique, First-principles calculations of electronic, optical and elastic Properties of Y₈CoIn₃, in *2014 International Conference on Electrical Engineering and Information & Communication Technology* (2014) pp. 1–4.
- [35] T. Bzdušek and M. Sigrist, Robust doubly charged nodal lines and nodal surfaces in centrosymmetric systems, *Phys. Rev. B* **96**, 155105 (2017).
- [36] J. Ahn and B.-J. Yang, Symmetry representation approach to topological invariants in C_{2v}-symmetric systems, *Phys. Rev. B* **99**, 235125 (2019).
- [37] A. Bouhon, T. Bzdušek, and R.-J. Slager, Geometric approach to fragile topology beyond symmetry indicators, *Phys. Rev. B* **102**, 115135 (2020).
- [38] S. Kobayashi and A. Furusaki, Fragile topological insulators protected by rotation symmetry without spin-orbit coupling, *Phys. Rev. B* **104**, 195114 (2021).
- [39] J. Ahn, D. Kim, Y. Kim, and B.-J. Yang, Band Topology and Linking Structure of Nodal Line Semimetals with Z₂ Monopole Charges, *Phys. Rev. Lett.* **121**, 106403 (2018).
- [40] J. Ahn, S. Park, and B.-J. Yang, Failure of Nielsen-Ninomiya Theorem and Fragile Topology in Two-Dimensional Systems with Space-Time Inversion Symmetry: Application to Twisted Bilayer Graphene at Magic Angle, *Phys. Rev. X* **9**, 021013 (2019).
- [41] A. A. Soluyanov and D. Vanderbilt, Computing topological invariants without inversion symmetry, *Phys. Rev. B* **83**, 235401 (2011).
- [42] R. Yu, X. L. Qi, A. Bernevig, Z. Fang, and X. Dai, Equivalent expression of Z₂ topological invariant for band insulators using the non-Abelian Berry connection, *Phys. Rev. B* **84**, 075119 (2011).
- [43] C. Fang, Y. Chen, H.-Y. Kee, and L. Fu, Topological nodal line semimetals with and without spin-orbital coupling, *Phys. Rev. B* **92**, 081201 (2015).
- [44] H. Gao, J. Strockoz, M. Frakulla, J. W. F. Venderbos, and H. Weng, Noncentrosymmetric topological Dirac semimetals in three dimensions, *Phys. Rev. B* **103**, 205151 (2021).
- [45] H. Gao, Y. Kim, J. W. F. Venderbos, C. L. Kane, E. J. Mele, A. M. Rappe, and W. Ren, Dirac-Weyl Semimetal: Coexistence of Dirac and Weyl Fermions in Polar Hexagonal ABC Crystals, *Phys. Rev. Lett.* **121**, 106404 (2018).
- [46] T. Zhang, D. Hara, and S. Murakami, Z₂ Dirac points with topologically protected multihelical surface states, *Phys. Rev. Res.* **4**, 033170 (2022).
- [47] T. Zhang and S. Murakami, Parallel and anti-parallel helical surface states for topological semimetals, *Scientific Reports* **13**, 9239 (2023).
- [48] J. P. Perdew and Y. Wang, Accurate and simple analytic representation of the electron-gas correlation energy, *Phys. Rev. B* **45**, 13244 (1992).
- [49] B. L. Gyorffy, A. J. Pindor, J. Staunton, G. M. Stocks, and H. Winter, A first-principles theory of ferromagnetic phase transitions in metals, *Journal of Physics F: Metal Physics* **15**, 1337 (1985).
- [50] B. L. Gyorffy, Coherent-Potential Approximation for a Nonoverlapping-Muffin-Tin-Potential Model of Random Substitutional Alloys, *Phys. Rev. B* **5**, 2382 (1972).
- [51] A. I. Liechtenstein, M. I. Katsnelson, and V. A. Gubanov, Exchange interactions and spin-wave stiffness in ferromagnetic metals, *Journal of Physics F: Metal Physics* **14**, L125 (1984).
- [52] G. Kresse and J. Furthmüller, Efficient iterative schemes for ab initio total-energy calculations using a plane-wave basis set, *Phys. Rev. B* **54**, 11169 (1996).
- [53] J. P. Perdew, K. Burke, and M. Ernzerhof, Generalized Gradient Approximation Made Simple, *Phys. Rev. Lett.* **77**, 3865 (1996).
- [54] G. Pizzi, V. Vitale, R. Arita, S. Blügel, F. Freimuth, G. Géranton, M. Gibertini, D. Gresch, C. Johnson, T. Koretsune, J. Ibañez-Azpiroz, H. Lee, J.-M. Lihm, D. Marchand, A. Marrazzo, Y. Mokrousov, J. I. Mustafa, Y. Nohara, Y. Nomura, L. Paulatto, S. Poncé, T. Ponweiser, J. Qiao, F. Thöle, S. S. Tsirkin, M. Wierzbowska, N. Marzari, D. Vanderbilt, I. Souza, A. A. Mostofi, and J. R. Yates, Wannier90 as a community code: new features and applications, *Journal of Physics: Condensed Matter* **32**, 165902 (2020).
- [55] F. Guinea, C. Tejedor, F. Flores, and E. Louis, Effective two-dimensional Hamiltonian at surfaces, *Phys. Rev. B* **28**, 4397 (1983).
- [56] M. P. L. Sancho, J. M. L. Sancho, and J. Rubio, Quick iterative scheme for the calculation of transfer matrices: application to Mo (100), *Journal of Physics F: Metal Physics* **14**, 1205 (1984).
- [57] M. P. L. Sancho, J. M. L. Sancho, J. M. L. Sancho, and J. Rubio, Highly convergent schemes for the calculation of bulk and surface Green functions, *Journal of Physics F: Metal Physics* **15**, 851 (1985).
- [58] Q. Wu, S. Zhang, H.-F. Song, M. Troyer, and A. A. Soluyanov, Wanniertools : An open-source software package for novel topological materials, *Computer Physics Communications* **224**, 405 (2018).
- [59] J. P. Perdew, A. Ruzsinszky, G. I. Csonka, O. A. Vydrov, G. E. Scuseria, L. A. Constantin, X. Zhou, and K. Burke, Restoring the Density-Gradient Expansion for Exchange in Solids and Surfaces, *Phys. Rev. Lett.* **100**, 136406 (2008).
- [60] N. Papanikolaou, R. Zeller, and P. Dederichs, Conceptual improvements of the KKR method, *Journal of Physics: Condensed Matter* **14**, 2799 (2002).
- [61] S. L. Dudarev, P. Liu, D. A. Andersson, C. R. Stanek, T. Ozaki, and C. Franchini, Parametrization of LSDA+U for noncollinear magnetic configurations: Multipolar magnetism in UO₂, *Phys. Rev. Mater.* **3**, 083802 (2019).
- [62] H. Ebert, D. Koedderitzsch, and J. Minar, Calculating condensed matter properties using the KKR-Green’s function method—recent developments and applications, *Reports on Progress in Physics* **74**, 096501 (2011).